

Simulation of Rare Events by the Stochastic Weighted Particle Method for the Boltzmann Equation

Sergej Rjasanow* and Wolfgang Wagner**

* University of Saarland, Department of Mathematics
Postfach 15 11 50, D-66041 Saarbrücken, Germany
email: rjasanow@num.uni-sb.de

** Weierstrass Institute for Applied Analysis and Stochastics
Mohrenstraße 39, D-10117 Berlin, Germany
email: wagner@wias-berlin.de

Abstract. An extension of the stochastic weighted particle method for the numerical treatment of the Boltzmann equation is presented. A new procedure for modelling the inflow boundary condition is introduced and its performance is tested in a two-dimensional example with strong density gradients. A gain factor in computing time of several orders of magnitude is achieved in specific situations.

Contents

1. Introduction	2
2. Stochastic Weighted Particle Method	4
2.1. Modelling of the boundary conditions	5
2.2. Modelling of the collisions	9
3. A two-dimensional test problem	10
3.1. Steady-state collisionless case	13
3.2. Surface functional	14
3.3. Volume functional	16
4. Numerical experiments	18
4.1. Evaluation of the surface functional	19
4.2. Evaluation of the volume functional	21
5. Conclusions	24
References	25

1. Introduction

In this paper we apply the Stochastic Weighted Particle Method (SWPM) to the numerical solution of the spatially two-dimensional Boltzmann equation. This method was introduced in [6], where we presented first numerical results for the one-dimensional heat exchange problem. The convergence of the method was investigated in [8], where we were also able to show an enormous reduction of the stochastic fluctuations using the SWPM for a model kinetic equation. In [7] we presented a detailed study of different effects of the numerical solution of this equation. The computation of macroscopic quantities in regions with low particle density was of special interest.

The **Boltzmann equation** for dilute monoatomic gases [3]

$$f_t + (v, \text{grad}_x f) = \int_{\mathbb{R}^3} \int_{S^2} B(v, w, e) [f(v')f(w') - f(v)f(w)] de dw \quad (1.1)$$

describes the time evolution of the particle density

$$f = f(t, x, v) : \mathbb{R}_+ \times \Omega \times \mathbb{R}^3 \rightarrow \mathbb{R}_+.$$

Here \mathbb{R}_+ denotes the set of non-negative real numbers and $\Omega \subset \mathbb{R}^d$, $d = 1, 2, 3$ is a domain in physical space. The following notations have been used:

- $v, w \in \mathbb{R}^3$ are the pre-collision velocities;
- $e \in S^2 \subset \mathbb{R}^3$ is a unit vector;
- v', w' are the post-collision velocities,
- $v' = \frac{1}{2}(v + w) + \frac{1}{2}|v - w|e, \quad w' = \frac{1}{2}(v + w) - \frac{1}{2}|v - w|e;$ (1.2)
- $B(v, w, e)$ is the collision kernel.

Note that the right-hand side of equation (1.1), known as the collision integral, depends on t and x only as parameters, so we have omitted this dependence in order not to overload the formulae. The collision kernel

$$B(v, w, e) = \frac{1}{2\sqrt{2} \pi \varepsilon} |v - w| = \frac{c_B}{4\pi} |v - w| \quad (1.3)$$

we will consider corresponds to the “hard spheres” model. The dimensionless parameter ε is the so-called Knudsen number, i.e. the quotient between the mean free path of the flow and the characteristic length of the problem.

The Boltzmann equation (1.1) is subjected to the **initial condition**

$$f(0, x, v) = f_0(x, v), \quad f_0 : \Omega \times \mathbb{R}^3 \rightarrow \mathbb{R}_+$$

as well as to some **boundary conditions** for $x \in \Gamma = \partial\Omega$. The boundary conditions usually prescribe the incoming flux of particles

$$f(t, x, v)(v, n_x), \quad x \in \Gamma, \quad v \in \mathbb{R}_{in}^3(x),$$

in terms of the outgoing flux of particles

$$f(t, x, w)|(w, n_x)|, \quad x \in \Gamma, \quad w \in \mathbb{R}_{out}^3(x),$$

where n_x denotes the unit **inward normal vector** to the boundary Γ , and the notations

$$\mathbb{R}_{in}^3(x) = \{w \in \mathbb{R}^3 : (w, n_x) > 0\}, \quad \mathbb{R}_{out}^3(x) = \{w \in \mathbb{R}^3 : (w, n_x) \leq 0\} \quad (1.4)$$

are used. The relation between incoming and outgoing flux is formulated using a so-called scattering kernel $r(t, x; w \rightarrow v)$ as follows (cf. [3, Ch. 8]):

$$f(t, x, v)(v, n_x) = \int_{\mathbb{R}_{out}^3(x)} r(t, x; w \rightarrow v) f(t, x, w) |(w, n_x)| dw, \quad (1.5)$$

$$x \in \Gamma, \quad v \in \mathbb{R}_{in}^3(x).$$

One example is the **specular reflection** with

$$r(t, x; w \rightarrow v) = \delta(w - (v - 2(v, n_x)n_x))$$

so that the boundary condition (1.5) takes the form

$$f(t, x, v) = f(t, x, v - 2(v, n_x)n_x), \quad x \in \Gamma, \quad v \in \mathbb{R}_{in}^3(x). \quad (1.6)$$

This boundary condition conserves the mass and the energy. The normal component of the bulk velocity is equal to zero on the boundary. The boundary condition (1.6) fulfils the reciprocity condition (see [3, Ch. 8] for more details) and therefore preserves the local equilibrium on the boundary. This boundary condition is usually inadequate for real surfaces but perfect for artificial boundaries due to spatial symmetry of the flow.

The next important example is the **diffuse reflection** with the Maxwellian distribution function

$$M_\Gamma(t, x, v) = \frac{1}{2\pi (RT_\Gamma(t, x))^2} \exp\left(-\frac{|v|^2}{2RT_\Gamma(t, x)}\right)$$

on the boundary Γ , normalised so that

$$\int_{\mathbb{R}_{in}^3(x)} M_\Gamma(t, x, w) (w, n_x) dw = 1,$$

where R is the gas constant. In this case the boundary condition (1.5) takes the form

$$f(t, x, v)(v, n_x) = F_{out}(t, x) M_\Gamma(t, x, v)(v, n_x), \quad x \in \Gamma, \quad v \in \mathbb{R}_{in}^3(x). \quad (1.7)$$

The connection between the outgoing and incoming flux of particles is such that the conservation of mass is guaranteed, i.e.

$$F_{out}(t, x) = \int_{\mathbb{R}_{out}^3(x)} f(t, x, w) |(w, n_x)| dw.$$

In general, the energy is not conserved by the boundary condition (1.7) but the local equilibrium is.

The third kind of boundary condition we will need is the so-called **inflow boundary condition**

$$f(t, x, v)(v, n_x) = f_{in}(t, x, v)(v, n_x), \quad x \in \Gamma, \quad v \in \mathbb{R}_{in}^3(x). \quad (1.8)$$

Here the incoming flux is prescribed independently of the outgoing flux which will therefore be adsorbed permanently.

The main aim of this paper is to model the incoming flux (1.8) using weighted particles in order to increase the accuracy of the numerical solution of the Boltzmann equation in certain regions of the flow. Usually those regions are “low density” regions where the resolution of the flow using standard particles is difficult or even impossible because of large stochastic fluctuations. We refer to [1], [4] for more detail on particle schemes and their applications, to [6] concerning additional references related to the stochastic weighted particle method, and to [2] concerning a related weighting scheme.

The paper is organised as follows. In Section 2 the structure of the stochastic weighted particle method is described. The simulation procedure for handling boundary conditions, in particular at the inflow boundary, is introduced in detail. A two-dimensional test problem is studied in Section 3. In the steady-state collisionless case analytic expressions are found for two specific functionals of the solution of the Boltzmann equation. Results of numerical experiments are presented in Section 4. The new facilities of the stochastic weighted particle method are demonstrated, reaching a gain factor in computing time of several orders of magnitude in specific examples.

2. Stochastic Weighted Particle Method

A system of simulation particles

$$\left(x_i(t), v_i(t), g_i(t)\right), \quad i = 1, \dots, n(t), \quad t \geq 0, \quad (2.1)$$

is used to approximate the behaviour of real gas. Here $x_i(t) \in \Omega$ and $v_i(t) \in \mathbb{R}^3$ denote respectively the position and the velocity of the i -th particle at time t and $g_i(t) > 0$ is some variable weight. The number of particles in the system is $n(t)$. The solution of the Boltzmann equation (1.1) is approximated in the sense that

$$\int_{\Omega} \int_{\mathbb{R}^3} \varphi(x, v) f(t, x, v) dv dx \quad \sim \quad \sum_{i=1}^{n(t)} g_i(t) \varphi(x_i(t), v_i(t)),$$

for appropriate test functions φ .

The time evolution of the particle system (2.1) is defined using a splitting technique. The simulation of the free flow of the particles and the simulation of their collisions are separated on a small time interval Δt . This means that on Δt , at a first step, the free flow is performed disregarding the possible collisions. Then, at a second step, the collisions are simulated neglecting the free flow.

During the free-flow simulation step, the particles move according to their velocities, i.e.

$$x_i(t + \Delta t) = x_i(t) + \int_t^{t+\Delta t} v_i(s) ds.$$

The velocities do not change unless a particle hits the boundary. In this case, the corresponding velocity changes according to the boundary conditions.

During the collision simulation step, a partition

$$\Omega = \bigcup_{l=1}^{N_{cell}} \Omega_l \quad (2.2)$$

of the spatial domain Ω into a finite number N_{cell} of disjoint cells is used. There is no interaction between different cells. Collisions of the particles are simulated in each cell.

2.1. Modelling of the boundary conditions

Here we describe the mechanism for the creation of new particles at the **inflow boundary** $\Gamma_{in} \subset \Gamma$ according to the boundary condition (1.8). We model the inflow by means of a Markov jump process.

The **waiting time parameter** is

$$\lambda^{(\beta)} = \int_{\Gamma_{in}} \int_{\mathbb{R}_{in}^3(x)} \beta(x, v) dv \sigma(dx), \quad (2.3)$$

where β is some **intensity function** not depending on the state of the system, $\mathbb{R}_{in}^3(x)$ is the half-space of directions showing inside the domain Ω (cf. (1.4)), and σ denotes the surface measure on Γ . This means that the waiting time τ until the next jump is determined from

$$\text{Prob}(\tau \geq t) = \exp(-t \lambda^{(\beta)}), \quad t \geq 0.$$

The **jump** of the system consists in the creation of a new particle at some point $x \in \Gamma_{in}$ with velocity $v \in \mathbb{R}_{in}^3(x)$, where x, v are distributed according to

$$\frac{1}{\lambda^{(\beta)}} \beta(x, v). \quad (2.4)$$

The weight of the new particle is determined by a **weight creation function** $\gamma(x, v)$.

The **inflow boundary condition** (1.8) prescribes the relationship between the functions β and γ as follows (assuming time homogeneity):

$$\gamma(x, v) \beta(x, v) = f_{in}(x, v) (v, n_x). \quad (2.5)$$

Note that there is considerable freedom in choosing the parameters which determine the mechanism for the creation of new particles at the inflow boundary.

The **average number of new particles** created during Δt is

$$\lambda^{(\beta)} \Delta t.$$

The **expected value of the weight of a new particle** is

$$\frac{1}{\lambda^{(\beta)}} \int_{\Gamma_{in}} \int_{\mathbb{R}_{in}^3(x)} \gamma(x, v) \beta(x, v) dv \sigma(dx) = \frac{F_{in}}{\lambda^{(\beta)}},$$

according to (2.5), where

$$F_{in} = \int_{\Gamma_{in}} \int_{\mathbb{R}_{in}^3(x)} f_{in}(x, v) (v, n_x) dv \sigma(dx). \quad (2.6)$$

The **expected overall weight** created during Δt is

$$\lambda^{(\beta)} \Delta t \frac{F_{in}}{\lambda^{(\beta)}} = F_{in} \Delta t \quad (2.7)$$

and does not depend on β . However, the **fluctuations** of the overall weight depend on the choice of the parameter. They are determined by the **second moment of the weight** of a new particle, which is

$$\frac{1}{\lambda^{(\beta)}} \int_{\Gamma_{in}} \int_{\mathbb{R}_{in}^3(x)} \gamma(x, v)^2 \beta(x, v) dv \sigma(dx). \quad (2.8)$$

In the following we consider the **special case** (cf. (2.6))

$$\beta(x, v) = \frac{F_{in}}{g_{in}} \left[\tilde{c} \tilde{p}(x, v) + c_{in} p_{in}(x, v) \right]$$

and

$$\gamma(x, v) = g_{in} \frac{p_{in}(x, v)}{\tilde{c} \tilde{p}(x, v) + c_{in} p_{in}(x, v)}, \quad (2.9)$$

where

$$\tilde{c} + c_{in} = 1, \quad \tilde{c}, c_{in} \geq 0,$$

and $g_{in} > 0$ is a **standard input weight**. The function

$$p_{in}(x, v) = \frac{f_{in}(x, v) (v, n_x)}{F_{in}} \quad (2.10)$$

describes the **main stream** at the inflow boundary, and the (probability density) function \tilde{p} describes some **auxiliary stream**. Note that (2.5) is satisfied.

The waiting time parameter (2.3) takes the form

$$\lambda^{(\beta)} = \frac{F_{in}}{g_{in}} \quad (2.11)$$

which does not depend on \tilde{c}, c_{in} . Position x and velocity v of the new particle are generated according to the distribution (2.4), i.e.

$$\tilde{c} \tilde{p}(x, v) + c_{in} p_{in}(x, v).$$

An upper bound for the weight (2.9) of a new particle is

$$g_{in} \min \left(\frac{1}{c_{in}}, \frac{1}{\tilde{c}} \sup_{x, v} \frac{p_{in}(x, v)}{\tilde{p}(x, v)} \right). \quad (2.12)$$

The second moment (2.8) of the weight takes the form

$$g_{in}^2 \int_{\Gamma_{in}} \int_{\mathbb{R}_{in}^3(x)} \frac{p_{in}(x, v)^2}{\tilde{c} \tilde{p}(x, v) + c_{in} p_{in}(x, v)} dv \sigma(dx).$$

The following **algorithm** is obtained:

0. Set time counter to zero.
1. Generate a time step with parameter (2.11) and add it to the time counter. If time counter exceeds Δt then STOP.
- 2a. With probability \tilde{c} create position and velocity (x, v) of the new particle according to the auxiliary stream \tilde{p} .
- 2b. With probability c_{in} create position and velocity (x, v) of the new particle according to the main stream p_{in} .
3. Determine the weight $\gamma(x, v)$ of the new particle according to (2.9).
4. Return to 1.

Remark 2.1 *If $g_{in} \sim n(0)^{-1}$ is small, then deterministic waiting times*

$$\frac{1}{\lambda^{(\beta)}} = \frac{g_{in}}{F_{in}}$$

can be used. This means that a deterministic number of particles is created. However, the stochastic mechanism is more stable in extreme situations (low particle numbers, large time steps, etc.).

Example 2.2 (Standard model) *In the cases $\tilde{c} = 0$ or $\tilde{p} = p_{in}$ position and velocity of the new particle are distributed according to the main stream p_{in} , and the weight (2.9) is g_{in} .*

Remark 2.3 *In the special case $c_{in} = 0$, all particles are created according to \tilde{p} with weight*

$$g_{in} \frac{p_{in}(x, v)}{\tilde{p}(x, v)}.$$

If \tilde{p} differs significantly from p_{in} , then only very few particles representing the main stream p_{in} will be created. However, those particles will have very large weights. The expected overall weight of particles created during a time interval of length Δt is as given in (2.7). However, its actual value fluctuates very strongly around this correct value, and is mostly too small. The effect of strongly fluctuating weights is not desirable since the value $\sup_{x,v} \gamma(x, v)$ controls the convergence.

Let

$$f_{in}(x, v) = M_{in}(x, v) = \frac{\varrho_{in}(x)}{(2\pi R T_{in}(x))^{3/2}} \exp\left(-\frac{|v - V_{in}(x)|^2}{2R T_{in}(x)}\right) \quad (2.13)$$

be the **inflow Maxwellian** describing the **main stream** flow at the **inflow boundary** Γ_{in} . Let \tilde{M} be some Maxwellian with arbitrary parameters $\tilde{\varrho}(x)$, $\tilde{V}(x)$ and $\tilde{T}(x)$ (cf. (2.13)) representing an **auxiliary stream** in a desired direction. Denote

$$\tilde{p}(x, v) = \frac{\tilde{M}(x, v)(v, n_x)}{\tilde{F}}, \quad (2.14)$$

where

$$\tilde{F} = \int_{\Gamma_{in}} \int_{\mathbb{R}_{in}^3(x)} \tilde{M}(x, v) (v, n_x) dv \sigma(dx).$$

The variable weight (2.9) takes the form (cf. (2.10))

$$g_{in} \frac{M_{in}(x, v)}{\frac{F_{in}}{\tilde{F}} \tilde{c} \tilde{M}(x, v) + c_{in} M_{in}(x, v)}.$$

One obtains (cf. (2.12))

$$\sup_{x, v} \frac{p_{in}(x, v)}{\tilde{p}(x, v)} = \frac{\tilde{F}}{F_{in}} \sup_{x, v} \frac{M_{in}(x, v)}{\tilde{M}(x, v)} \quad (2.15)$$

and

$$\frac{M_{in}(x, v)}{\tilde{M}(x, v)} = \frac{\varrho_{in}(x)}{\tilde{\varrho}(x)} \frac{\tilde{T}(x)^{3/2}}{T_{in}(x)^{3/2}} \exp \left(-\frac{|v - V_{in}(x)|^2}{2R T_{in}(x)} + \frac{|v - \tilde{V}(x)|^2}{2R \tilde{T}(x)} \right).$$

The expression (2.15) is bounded with respect to v if

$$\tilde{T}(x) > T_{in}(x) \geq \kappa \tilde{T}(x), \quad \tilde{\varrho}(x) \geq \kappa \varrho_{in}(x), \quad \text{for some } \kappa > 0.$$

If the parameters of the inflow Maxwellian (2.13) as well as the normal vector $n_x = n$ do not depend on $x \in \Gamma_{in}$ then (cf. (2.6), (1.4))

$$F_{in} = |\Gamma_{in}| \int_{(v, n) > 0} M_{in}(v) (v, n) dv$$

and

$$p_{in}(x, v) = \frac{1}{|\Gamma_{in}|} \frac{M_{in}(v) (v, n)}{\int_{(v, n) > 0} M_{in}(v) (v, n) dv}, \quad (2.16)$$

where $|\Gamma_{in}|$ denotes the area of Γ_{in} . According to (2.16), the position of the new particle is generated uniformly on Γ_{in} , and the distribution of its velocity is

$$\frac{M_{in}(v) (v, n)}{\int_{(v, n) > 0} M_{in}(v) (v, n) dv}, \quad (v, n) > 0.$$

The integral in (2.16) can easily be computed analytically

$$\int_{(v, n) > 0} M_{in}(v) (v, n) dv = \quad (2.17)$$

$$\frac{\varrho_{in}}{2} (V_{in}, n) \left[1 + \operatorname{erf} \left(\frac{(V_{in}, n)}{\sqrt{2R T_{in}}} \right) \right] + \varrho_{in} \sqrt{\frac{R T_{in}}{2\pi}} \exp \left(-\frac{(V_{in}, n)^2}{2R T_{in}} \right),$$

where

$$\begin{aligned} \operatorname{erf}(a) &= \frac{2}{\sqrt{\pi}} \int_0^a \exp(-z^2) dz = \frac{1}{\sqrt{2\pi}} \int_{-a\sqrt{2}}^{a\sqrt{2}} \exp\left(-\frac{y^2}{2}\right) dy, \quad a \geq 0, \\ \operatorname{erf}(a) &= \operatorname{erf}(-a), \quad a < 0. \end{aligned} \quad (2.18)$$

Note that, in the case $V_{in} = 0$, (2.17) takes the form

$$\int_{(v,n)>0} M_{in}(v)(v,n) dv = \varrho_{in} \sqrt{\frac{RT_{in}}{2\pi}}$$

and the corresponding normalisation factor is

$$\frac{1}{(2\pi RT_{in})^{3/2}} \sqrt{\frac{2\pi}{RT_{in}}} = \frac{1}{2\pi (RT_{in})^2}.$$

2.2. Modelling of the collisions

The collision-simulation procedure for systems of weighted particles has been described in detail elsewhere (see [6], [8]). Here we mention the main steps.

The state of the system is

$$z = \left((x_1, v_1, g_1), \dots, (x_n, v_n, g_n) \right).$$

During a collision two new particles with equal weights and post-collision velocities (1.2) are created,

$$(x_i, v'_i, \min(g_i, g_j)), \quad (x_j, v'_j, \min(g_i, g_j)).$$

The collision partners lose a corresponding part of their weights,

$$(x_i, v_i, g_i - \min(g_i, g_j)), \quad (x_j, v_j, g_j - \min(g_i, g_j)).$$

Particles with zero weights are removed from the system. Thus, the number of particles in the systems remains constant if two particles of equal weight collide, and increases by one if the two colliding particles have different weights.

The collision mechanism is described by a Markov jump process. The waiting time parameter is (cf. (1.3))

$$\hat{\pi}(z) = \frac{1}{|\Omega_l|} c_B \frac{1}{2} U_{l,max} (n_l - 1) [2 g_{sum}(z) - n_l g_{min}(z)],$$

where $g_{min}(z)$ is a lower bound of the weights in the cell, i.e.

$$g_{min}(z) \leq g_i, \quad \forall i : x_i \in \Omega_l,$$

$$g_{sum}(z) = \sum_{i : x_i \in \Omega_l} g_i$$

is the local mass, n_l denotes the number of particles in the cell, and $U_{l,max}$ is some upper bound of the relative velocities in the cell.

The index i is chosen according to

$$\frac{g_i (n_l - 2) + g_{sum}(z) - (n_l - 1) g_{min}(z)}{(n_l - 1) [2 g_{sum}(z) - n_l g_{min}(z)]}.$$

Given i , the parameter j is chosen according to

$$\frac{g_i + g_j - g_{min}(z)}{g_i (n_l - 2) + g_{sum}(z) - (n_l - 1) g_{min}(z)}.$$

The jump is fictitious with probability

$$1 - \frac{|v_i - v_j|}{U_{l,max}} \frac{\max(g_i, g_j)}{g_i + g_j - g_{min}(z)}.$$

The vector e is uniformly distributed on the unit sphere S^2 .

3. A two-dimensional test problem

The two-dimensional domain Ω we will use for our numerical experiments is a trapezoid

$$\Omega = \{x = (x_1, x_2)^T \in \mathbb{R}^2, 0 < x_1 < a, 0 < x_2 < b + x_1 \tan(\alpha)\}$$

as shown in **Figure 3.1**.

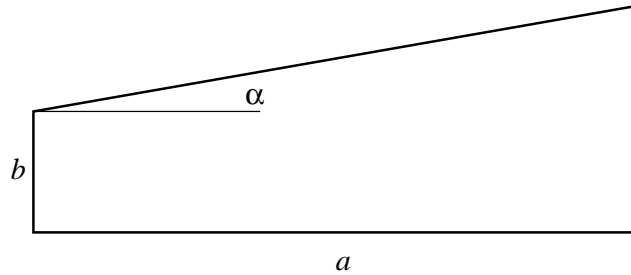


Figure 3.1 Computational domain Ω

The boundary Γ of the domain Ω consists of four straight pieces

$$\Gamma = \Gamma_l \cup \Gamma_b \cup \Gamma_r \cup \Gamma_t \tag{3.1}$$

corresponding to the left, bottom, right and top parts of the boundary. The unit inward normal vectors to these parts of the boundary are

$$n_l = (1, 0, 0)^T, \quad n_b = (0, 1, 0)^T, \quad n_r = (-1, 0, 0)^T, \quad n_t = (\sin(\alpha), -\cos(\alpha), 0)^T. \tag{3.2}$$

An incoming flux of the particles is prescribed on the left part of the boundary Γ_l corresponding to the boundary condition (1.8) with (cf. (2.13))

$$f_{in}(t, x, v) = \frac{\varrho_{in}}{(2\pi RT_{in})^{3/2}} \exp\left(-\frac{|v - V_{in}|^2}{2RT_{in}}\right), \quad t > 0, \quad x \in \Gamma_l, \quad (v, n_l) > 0. \tag{3.3}$$

We assume that the parameters of the Maxwell distribution (3.3) ρ_{in} , V_{in} and T_{in} are constant with respect to time and space variables. Furthermore, we will simulate the situation where the temperature of the inflow is low ($T_{in} = 10^\circ - 20^\circ K$) and at the same time the Mach number (the ratio of the stream speed to the speed of sound)

$$\text{Mach} = \frac{|V_{in}|}{\sqrt{\gamma R T_{in}}}$$

is rather high (Mach = 5 – 20).

The boundary piece Γ_b will usually represent the axis of symmetry, so we have to use the specular reflection (1.6) there.

At the boundary Γ_r we will assume a permanent adsorption of the particles. This means that

$$f(t, x, v)(v, n_r) = 0, \quad t > 0, \quad x \in \Gamma_r, \quad (v, n_r) > 0.$$

In other words we are modelling the “outflow” of the particles.

On the top of the computational domain the diffuse reflection of particles (1.7) will usually be assumed. The corresponding temperature of this boundary T_t will be much higher than that of the inflow.

The test problem described above is simple but already sufficient to illustrate the new possibilities arising from the introduction of weights to the stochastic particle schemes.

A first interesting test is an adequate computation of the influence of the “hot” top of the domain on the flow. The main problem here is a big difference in density along a line from the bottom to the top. If the Mach number is, for instance, Mach = 10 then the density changes from the value close to ρ_{in} in the neighbourhood of the bottom to 10^{-4} times this value at the top. In computational practice this means that only very few particles will reach the hot top of the domain and then turn back to the flow. The picture of the flow will be stochastically fluctuated by those particles. An enormous amount of smoothing steps would be necessary to work out the real influence of the hot top. However, this influence can be very important because of the heating of the main stream. In the next two figures we illustrate this effect.

In **Figure 3.2** we show the contours of the density, temperature, local Mach number as well as of the local equilibrium function

$$\text{Crit}(t, x) = \frac{1}{\rho R T} \sqrt{\frac{2}{5} \frac{|q|^2}{R T} + \frac{1}{2} \|M - \rho V V^T - p I\|_F^2}. \quad (3.4)$$

The function (3.4) was introduced in [9] and describes a weighted deviation of the local distribution function from the Maxwell distribution having the corresponding macroscopic parameters. The vector q in (3.4) is the heat flux vector

$$q(t, x) = \frac{1}{2} \int_{\mathbb{R}^3} (v - V) |v - V|^2 f(t, x, v) dv,$$

M denotes the momentum flow

$$M(t, x) = \int_{\mathbb{R}^3} v v^T f(t, x, v) dv,$$

V is the bulk velocity

$$\varrho(t, x)V(t, x) = \int_{\mathbb{R}^3} v f(t, x, v) dv,$$

p is the pressure

$$p(t, x) = \varrho(t, x)RT(t, x)$$

and $\|\cdot\|_F$ denotes the Frobenius norm of a matrix.

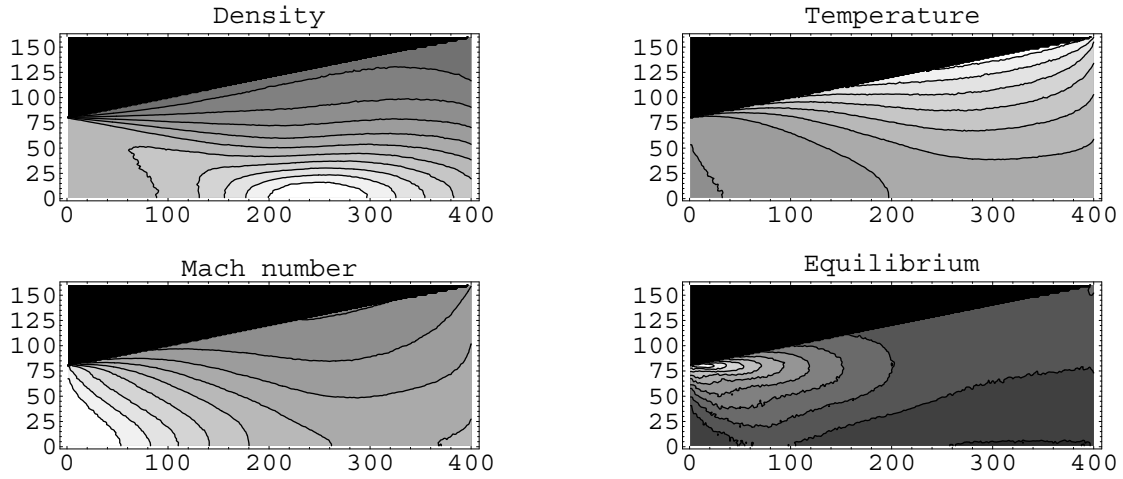


Figure 3.2 Contour plot of the macroscopic quantities.

The input parameters of this test are: $a = 2.0$, $b = 0.4$, $\alpha = 0.2$. We have used the inflow parameters (cf. (3.3))

$$\varrho_{in} = 1.0, V_{in} = (294.39, 0, 0)^T, T_{in} = 10.0,$$

and diffuse reflection with $T_t = 300.0$ on Γ_t . The inflow velocity in (3.5) corresponds to the Mach number equal to 5.0. We have used the mean free path value $\varepsilon = 0.1$ for this simulation.

The absolute values of the depicted results can be seen in **Figure 3.3** where we show the same macroscopic quantities plotted along the axis of symmetry (i.e. $x_2 = 0$).

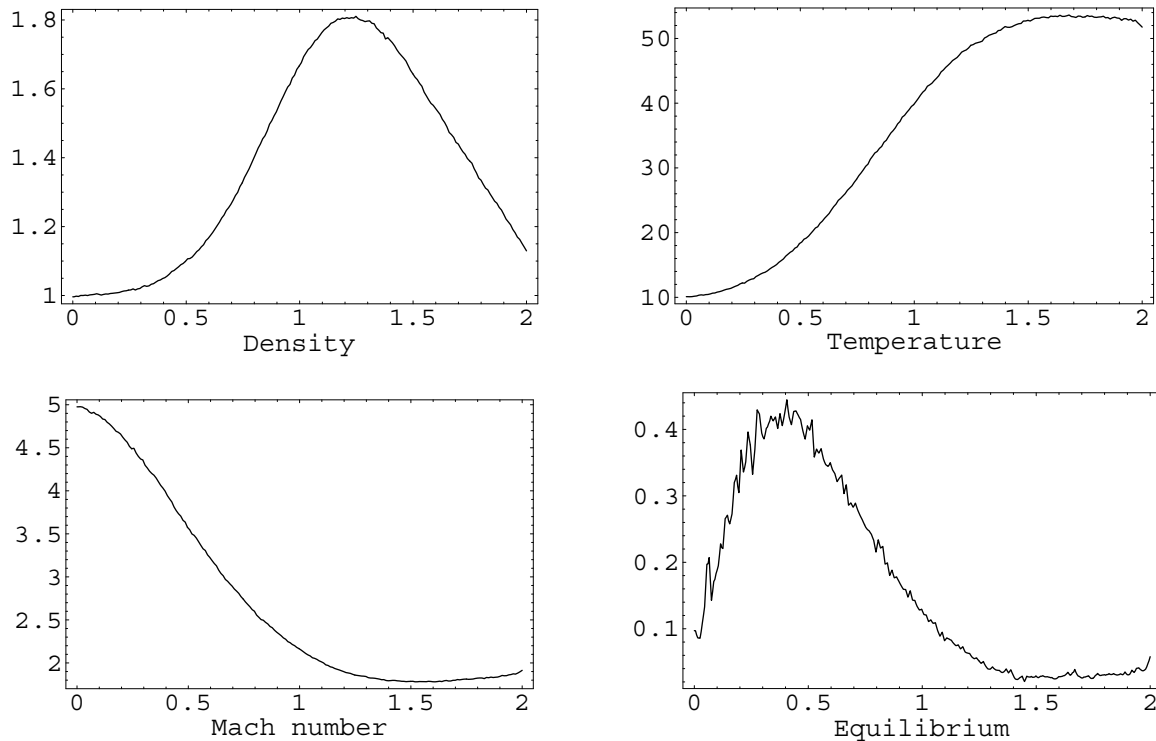


Figure 3.3 The macroscopic quantities on the line of symmetry.

These relatively smooth figures (except the function $\text{Crit}(t, x)$ which involves third moments) were obtained using 6400 averaging time steps after reaching the “steady-state” situation.

Similar results can be obtained for $\text{Mach} = 10$ using many more averaging steps. However, it is almost impossible to see any effects of the “hot” top boundary (even if it becomes artificially very hot) for $\text{Mach} = 15$. The particle density close to the top is about 10^{-8} times the inflow density.

An important step towards handling this problem is the accurate computation of the following functionals of the solution of the Boltzmann equation. The first functional describes the flow of the particles through the top of the computational domain Γ_t . The second functional is the density of the gas along the line Γ_r . In order to ensure precision in our tests we find in the subsequent subsections the analytical expressions for these functionals in the collisionless steady-state situation.

3.1. Steady-state collisionless case

Consider a special steady-state model problem for the function $f(x, v)$ satisfying the free flow equation

$$(v, \text{grad}_x f(x, v)) = 0, \quad x_1 > 0, \quad v_1 > 0. \quad (3.5)$$

The equation (3.5) is subjected to the boundary condition (cf. (1.8))

$$f(x, v) = f_{in}(x, v), \quad x_1 = 0, \quad v_1 > 0.$$

The inflow function $f_{in}(x, v)$ vanishes outside the strip

$$\Gamma_{in} = \{x \in \mathbb{R}^3, x_1 = 0, 0 \leq x_2 \leq b, -\infty < x_3 < \infty\}$$

having the form

$$f_{in}(x, v) = \begin{cases} M_{in}(v) & , \quad x_1 = 0, 0 \leq x_2 \leq b, \\ 0 & , \quad \text{otherwise.} \end{cases} \quad (3.6)$$

The Maxwell distribution function with constant parameters ϱ_{in} , $V_{in} = (V, 0, 0)^T$ and T_{in} is (cf. (2.13))

$$M_{in}(v) = \frac{\varrho_{in}}{(2\pi RT_{in})^{3/2}} \exp\left(-\frac{|v - V_{in}|^2}{2RT_{in}}\right). \quad (3.7)$$

The solution of the boundary value problem (3.5), (3.6) is given by the formula

$$f(x, v) = f_{in}(x + \tau v, v), \quad \tau \in \mathbb{R}, \quad (3.8)$$

where

$$\tau = \tau(x, v) = -\frac{x_1}{v_1}, \quad v_1 > 0, \quad (3.9)$$

so that $x_1 + \tau v_1 = 0$.

3.2. Surface functional

In this subsection we consider the problem of calculating the functional of the solution

$$Q(s) = \int_{\Gamma_t(s)} \int_{\mathbb{R}_{out}^3(x)} f(x, v) |(v, n_x)| dv \sigma(dx), \quad s > 0, \quad (3.10)$$

i.e. the number of particles crossing the rectangular “outflow” boundary

$$\Gamma_t(s) = \{x \in \mathbb{R}^3, x = (u, b + \tan(\alpha)u, w)^T, 0 \leq u \leq s, 0 \leq w \leq 1\} \quad (3.11)$$

per unit of time. The surface measure can be expressed as

$$\sigma(dx) = J_x(u, w) du dw = \sqrt{\left|\frac{\partial x}{\partial u}\right|^2 \left|\frac{\partial x}{\partial w}\right|^2 - \left(\frac{\partial x}{\partial u}, \frac{\partial x}{\partial w}\right)^2} du dw.$$

Using (3.11) we obtain

$$\sigma(dx) = \sqrt{1 + \tan^2(\alpha)} du dw = \frac{1}{\cos(\alpha)} du dw.$$

The normal vector to $\Gamma_t(s)$ is constant and has the form (cf. (3.2))

$$n_t = (\sin(\alpha), -\cos(\alpha), 0)^T. \quad (3.12)$$

The integration domain in velocity space (inner integral in (3.10)) is reduced according to the constraints (cf. (1.4), (3.8), (3.6))

$$(v, n_t) \leq 0, \quad 0 \leq x_2 + \tau v_2 \leq b,$$

or equivalently (cf. (3.12), (3.9))

$$v_1 \sin(\alpha) - v_2 \cos(\alpha) \leq 0, \quad 0 \leq x_2 - \frac{v_2}{v_1} x_1 \leq b.$$

These inequalities are fulfilled if

$$v \in \mathbb{R}_+^3(x) = \left\{ v_1 > 0, \tan(\alpha)v_1 \leq v_2 \leq \left(\tan(\alpha) + \frac{b}{x_1} \right) v_1 \right\}.$$

Thus, the functional (3.10) simplifies to

$$Q(s) = \frac{1}{\cos(\alpha)} \int_0^1 dw \int_0^s du \int_{\mathbb{R}_+^3(x)} f_M(v)(v, n_t) dv$$

and can be written as

$$\frac{\rho_{in}}{(2\pi RT_{in})^{3/2}} \int_0^s du \int_{\mathbb{R}_+^3(x)} \exp\left(-\frac{(v_1 - V)^2 + v_2^2 + v_3^2}{2RT_{in}}\right) \frac{(v, n_t)}{\cos(\alpha)} dv. \quad (3.13)$$

The integration over v_3 can be done immediately

$$\int_{-\infty}^{\infty} \exp\left(-\frac{v_3^2}{2RT_{in}}\right) dv_3 = \sqrt{2\pi RT_{in}}.$$

Thus, the velocity integral is now

$$\int_0^{\infty} dv_1 \int_{v_1 \tan(\alpha)}^{v_1(\tan(\alpha) + b/x_1)} \exp\left(-\frac{(v_1 - V)^2 + v_2^2}{2RT_{in}}\right) (-\tan(\alpha)v_1 + v_2) dv_2. \quad (3.14)$$

Then we use the following substitution in (3.14)

$$\begin{aligned} v_1 &= z_1 \sqrt{2RT_{in}}, & dv_1 &= \sqrt{2RT_{in}} dz_1, \\ v_2 &= z_2 \sqrt{2RT_{in}}, & dv_2 &= \sqrt{2RT_{in}} dz_2, \end{aligned}$$

where new (dimensionless) variables satisfy

$$z_1 \in (0, \infty), \quad z_2 \in (c(z_1), d(z_1, u)) = (z_1 \tan(\alpha), z_1(\tan(\alpha) + b/x_1)).$$

Thus, with

$$\xi = \frac{V}{\sqrt{2RT_{in}}}$$

we get the following expression

$$(2RT_{in})^{3/2} \int_0^{\infty} e^{-(z_1 - \xi)^2} \left(\int_{c(z_1)}^{d(z_1, u)} (-c(z_1)e^{-z_2^2} + z_2 e^{-z_2^2}) dz_2 \right) dz_1.$$

Calculating the integral over z_2 and using (3.13) we obtain the function (cf. (2.18))

$$q(u) = -\frac{\rho_{in}}{2\pi} \sqrt{2RT_{in}} \int_0^\infty e^{-(z_1-\xi)^2} \left(\sqrt{\pi} c(z_1) \operatorname{erf}(z_2) + e^{-z_2^2} \right) \Big|_{z_2=c(z_1)}^{d(z_1,u)} dz_1 \quad (3.15)$$

and therefore

$$Q(s) = \int_0^s q(u) du. \quad (3.16)$$

Consider the special case $\alpha = 0$. Then

$$c(z_1) = 0, \quad d(z_1, u) = z_1 \frac{b}{u}$$

and the function $q(u)$ simplifies to

$$q(u) = \frac{\rho_{in}}{2\pi} \sqrt{2RT_{in}} \int_0^\infty e^{-(z_1-\xi)^2} \left(1 - e^{-z_1^2 \frac{b^2}{u^2}} \right) dz_1. \quad (3.17)$$

The integration in (3.17) can now be done analytically and we get

$$q(u) = \frac{\rho_{in} \sqrt{2RT_{in}}}{4\sqrt{\pi}} \left(1 + \operatorname{erf}(\xi) - \frac{u}{\sqrt{b^2 + u^2}} e^{-\frac{\xi^2 b^2}{b^2 + u^2}} \left(1 + \operatorname{erf} \left(\frac{\xi u}{\sqrt{b^2 + u^2}} \right) \right) \right). \quad (3.18)$$

Further simplification can be achieved if we assume that

$$\alpha = 0, \quad \xi = 0.$$

This case corresponds to the zero average velocity V_{in} in (3.7). The function $q(u)$ is now

$$q(u) = \frac{\rho_{in}}{4\sqrt{\pi}} \sqrt{2RT_{in}} \left(1 - \frac{u}{\sqrt{b^2 + u^2}} \right) \quad (3.19)$$

and can be integrated analytically

$$Q(s) = \frac{\rho_{in}}{4\sqrt{\pi}} \sqrt{2RT_{in}} \left(b + s - \sqrt{b^2 + s^2} \right). \quad (3.20)$$

This gives us some test curves for different settings of parameters. The general case (3.15) requires a numerical integration procedure while the curves (3.18) and (3.19) can be used directly.

3.3. Volume functional

We now consider the same model boundary value problem as in the previous subsection, and compute the density $\rho(x)$ for x from the ‘‘outflow’’ boundary Γ_τ . This part of the boundary is described via parametrisation

$$\begin{pmatrix} a \\ 0 \end{pmatrix} + x_2 \begin{pmatrix} 0 \\ 1 \end{pmatrix}, \quad 0 \leq x_2 \leq b + a \tan(\alpha). \quad (3.21)$$

Thus the density $\varrho(x)$ is a function of x_2 alone.

The solution of the problem is given by (3.8). Our task now is to find an analytical expression for the density

$$\varrho(x) = \int_{\mathbb{R}^3} f(x, v) dv = \int_{\mathbb{R}_+^3(x)} M_{in}(v) dv, \quad x \in \Gamma_r.$$

The integration domain $\mathbb{R}_+^3(x)$ is defined according to the constraints (cf. (3.9))

$$v_1 > 0, \quad x_1 + \tau v_1 = 0, \quad 0 \leq x_2 + \tau v_2 \leq b$$

or equivalently

$$v_1 > 0, \quad \frac{x_2 - b}{x_1} \leq \frac{v_2}{v_1} \leq \frac{x_2}{x_1}. \quad (3.22)$$

Thus for positive v_1 (3.22) results in

$$\frac{x_2 - b}{x_1} v_1 \leq v_2 \leq \frac{x_2}{x_1} v_1$$

and we get

$$\varrho(x) = \int_0^\infty dv_1 \int_{\frac{x_2-b}{x_1} v_1}^{\frac{x_2}{x_1} v_1} dv_2 \int_{-\infty}^\infty f_M(v) dv_3.$$

The integral with respect to v_3 can be computed immediately and we obtain

$$\varrho(x) = \frac{\varrho_{in}}{2\pi R T_{in}} \int_0^\infty \exp\left(-\frac{(v_1 - V)^2}{2 R T_{in}}\right) dv_1 \int_{\frac{x_2-b}{x_1} v_1}^{\frac{x_2}{x_1} v_1} \exp\left(-\frac{v_2^2}{2 R T_{in}}\right) dv_2. \quad (3.23)$$

The substitution $v_1 = \sqrt{2 R T_{in}} z_1$ and $v_2 = \sqrt{2 R T_{in}} z_2$ in (3.23) leads to

$$\begin{aligned} \varrho(x) &= \frac{\varrho_{in}}{\pi} \int_0^\infty \exp(-(z_1 - \xi)^2) dz_1 \int_{\frac{x_2-b}{x_1} z_1}^{\frac{x_2}{x_1} z_1} \exp[-z_2^2] dz_2 \\ &= \frac{\varrho_{in}}{2\sqrt{\pi}} \int_0^\infty \exp(-(z_1 - \xi)^2) \left(\operatorname{erf}\left(\frac{x_2}{x_1} z_1\right) - \operatorname{erf}\left(\frac{x_2 - b}{x_1} z_1\right) \right) dz_1, \end{aligned}$$

where

$$\xi = \frac{V}{\sqrt{2 R T_{in}}}.$$

Thus, we get

$$\varrho(x) = \frac{\varrho_{in}}{2\sqrt{\pi}} \int_0^\infty \left(\exp(-(z_1 - \xi)^2) \right) \left(\operatorname{erf}\left(\frac{x_2}{x_1} z_1\right) - \operatorname{erf}\left(\frac{x_2 - b}{x_1} z_1\right) \right) dz_1. \quad (3.24)$$

Further simplification is possible if $\xi = 0$. In this case we use

$$\int_0^\infty \exp(-z^2) \operatorname{erf}(yz) dz = \frac{1}{\sqrt{\pi}} \arctan y$$

and obtain

$$\varrho(x) = \frac{\varrho_{in}}{2\pi} \left(\arctan \frac{x_2}{x_1} - \arctan \frac{x_2 - b}{x_1} \right).$$

4. Numerical experiments

In this section we report the results of our computer tests for the numerical computation of the surface and volume functionals formulated above. The main result we present is the reduction of the stochastical fluctuations using particles with weights. We employ the modelling procedure from Section 2 for the incoming flux of the particles in order to follow certain preferred directions.

We use the uniform discretisation of the computational domain in a number of rectangular cells as shown in **Figure 4.1**.

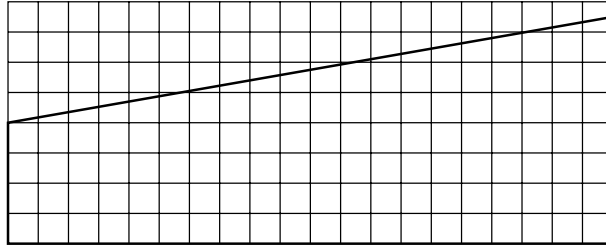


Figure 4.1 Discretisation of the computational domain Ω

The geometrical parameters of the computational domain are

$$a = 2.0, \quad b = 0.4, \quad \alpha = 0.3 .$$

The discretisation parameters are

$$N_{x_1} = 100, \quad N_{x_2} = 51 ,$$

so that $N_{cell} = N_{x_1} N_{x_2}$ (cf. (2.2)).

The boundary conditions are chosen so that the analytic curves for the functionals in the steady-state free-flow case are valid. Thus we use the inflow on Γ_l , the specular reflection on Γ_b and the adsorption on Γ_r and Γ_t . The temperature of the inflow is set at $T_{in} = 10$.

The following auxiliary streams are used for the modelling of the surface and volume functionals. The generating Maxwell distribution for the auxiliary streams (cf. (2.14)) differs from the Maxwell distribution of the input flow only by the direction of the bulk velocity \tilde{V} , i.e.

$$\tilde{M}(v) = \frac{\rho_{in}}{(2\pi RT_{in})^{3/2}} \exp\left(-\frac{|v - \tilde{V}|^2}{2RT_{in}}\right).$$

The bulk velocity \tilde{V} is obtained by rotation of the V_{in} , i.e.

$$\tilde{V} = |V_{in}|(\cos(\Phi), \sin(\Phi), 0)^T.$$

The angle $\Phi_1 = \arctan(b/a + \tan(\alpha))$ is chosen for the surface functional as shown in the left plot of **Figure 4.2**. The angle $\Phi_2 = \alpha$ is chosen for the volume functional (right plot in **Figure 4.2**).

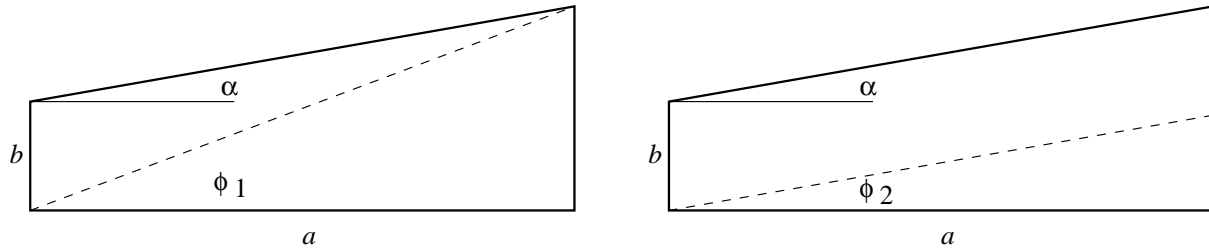


Figure 4.2 Directions of the auxiliary streams

The probability density (2.14) of the auxiliary stream is then given by (cf. (2.16), (3.1), (3.2))

$$\tilde{p}(x, v) = \frac{1}{|\Gamma_l|} \frac{\tilde{M}(v)(v, n_l)}{\int_{(v, n_l) > 0} \tilde{M}(v)(v, n_l) dv}, \quad x \in \Gamma_l, \quad v_1 > 0.$$

4.1. Evaluation of the surface functional

In this subsection we present the results of numerical tests obtained for the standard particle method with constant weights in comparison with the SWPM. The aim is to compute the functional (3.10) for different settings of parameters. The most interesting parameter of the simulation is the Mach number. It is clear that the number of particles crossing the top boundary Γ_t of the computational domain decreases drastically with an increasing Mach number and with the increasing distance from the inflow boundary Γ_l . This situation only occurs, of course, if $\alpha > 0$. For the straight pipe it was no problem to compute the functional (3.10) using standard particles even for a Mach number equal to 15.

We begin our tests with the modelling of the steady-state free-flow situation where the analytical solutions (3.16), (3.15), (3.18) and (3.20) are available. We first consider a relatively small Mach number, Mach = 1. The results of the computations after 100 averaging steps are presented in **Figure 4.3**.

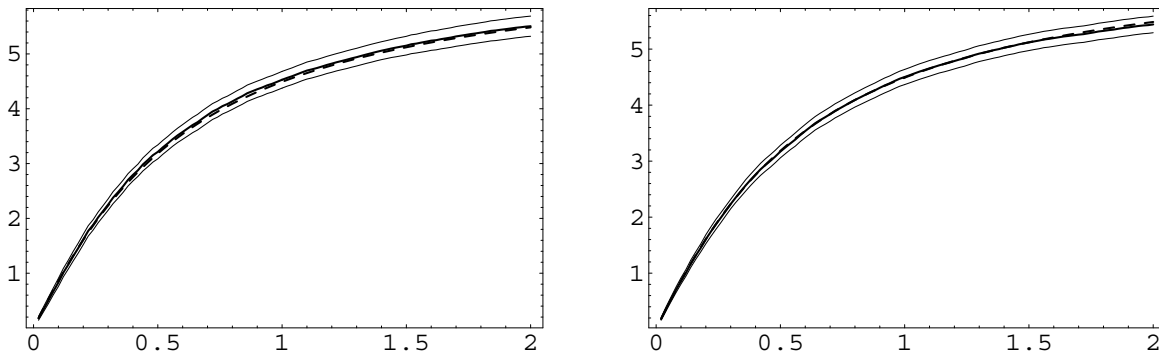


Figure 4.3 Exact solution, empirical mean and confidence intervals for the Mach number 1 using 100 averaging steps.

In these plots the dashed line represents the analytical solution (3.15), (3.16). The thick solid line on the left plot represents the empirical mean obtained by the standard scheme,

and on the right plot that obtained by the weighted scheme with parameters $\tilde{c} = c_{in} = 0.5$. The thin solid lines represent the corresponding confidence intervals. It is clear to see that the standard scheme is as good as the weighted scheme for this low Mach number.

The situation changes drastically for Mach = 10 as shown in **Figure 4.4**.

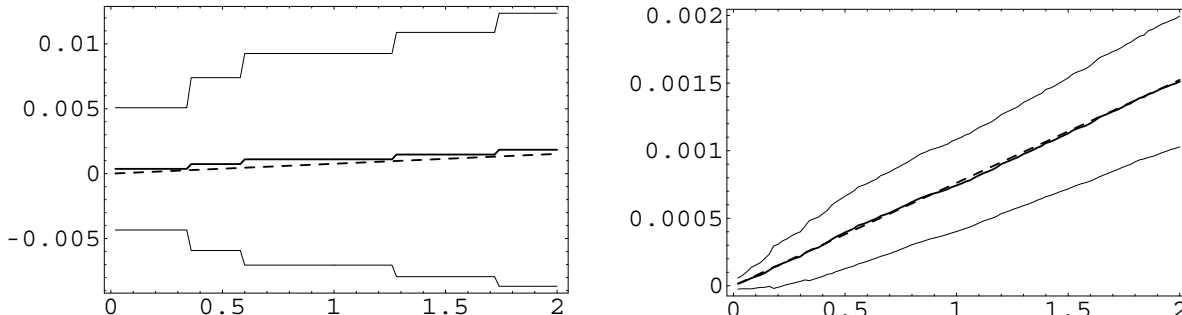


Figure 4.4 Exact solution, empirical mean and confidence intervals for the Mach number 10 using 1600 averaging steps.

Here we have used 1600 averaging steps for both methods. The weighted scheme does very well and delivers a reasonably accurate numerical solution (right plot in **Figure 4.4**) while the standard scheme gives only a very rough estimate (left plot in **Figure 4.4**). Note the different scales in these plots.

If we model collisions then the weighted scheme becomes more expensive. A fair test in this situation is obtained in the following way. We increase the number of averaging steps of the standard scheme step by step, watching the accuracy until that of the weighted scheme is reached. Then we compare the computational times required. The following results were obtained for Mach = 10 and the mean free path $\varepsilon = 0.5$. The weighted scheme needs 1.8 times more computational time per averaging step than the standard scheme. On the other hand we need 409600 averaging steps for the standard scheme to reach the accuracy of the weighted scheme after 1600 averaging steps. This means that for this example the weighted scheme is about 140 times “faster” than the standard scheme. The results of this numerical test are presented in **Figure 4.5**.

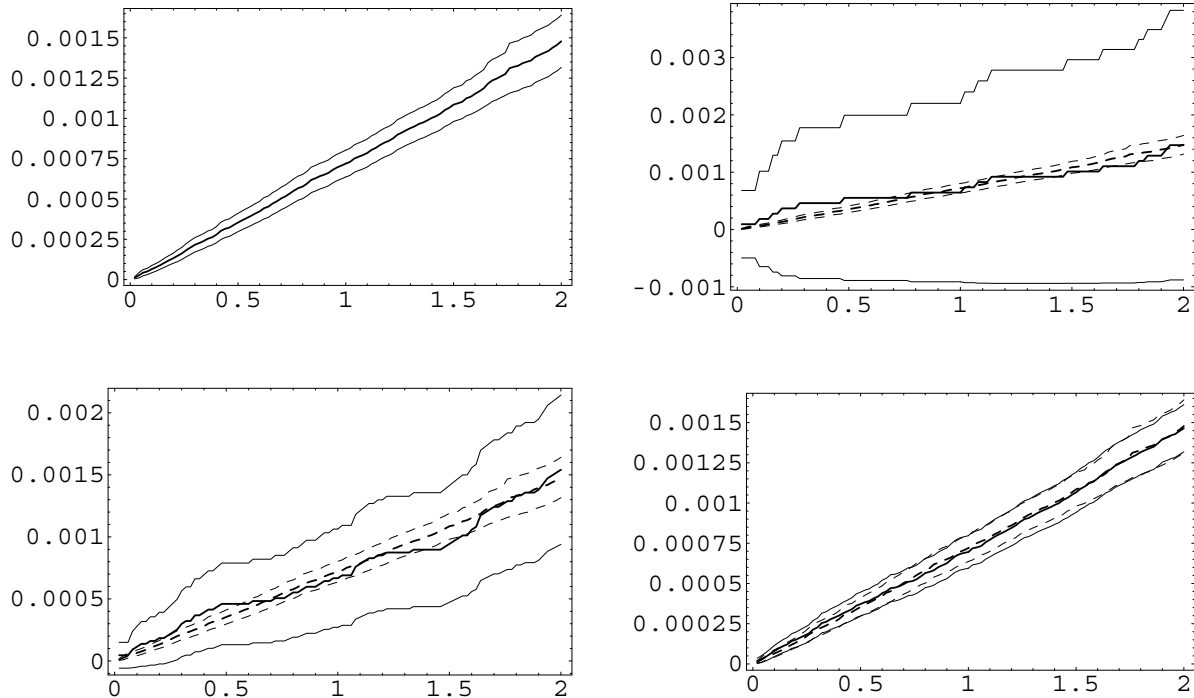


Figure 4.5 Empirical mean and confidence intervals for the Mach number 10 using 1600 averaging steps for the weighted scheme and 1600, 25600, 409600 averaging steps for the standard scheme.

The upper-left plot presents the empirical mean and confidence intervals for the weighted scheme. The dashed lines on the other plots reproduce these results for comparison with the results of the standard scheme. The upper-right plot corresponds to 1600 averaging steps, the lower-left plot to 25600 and the lower-right plot to 409600 averaging steps of the standard scheme. It is clear to see that for 409600 averaging steps the quality of the numerical solution becomes comparable.

4.2. Evaluation of the volume functional

In this subsection we compute the density $\rho(x)$ for x from the “outflow” boundary Γ_r . We first consider the free-flow case with Mach = 10. The density changes in this example from the value 0.8 on the axis of symmetry to 10^{-4} on the top of the computational domain. In **Figure 4.6** we plot the analytical density (3.24), the numerical empirical mean value obtained after 100 averaging steps of the weighted method with the parameters $\tilde{c} = c_{in} = 0.5$ as well the corresponding confidence intervals.

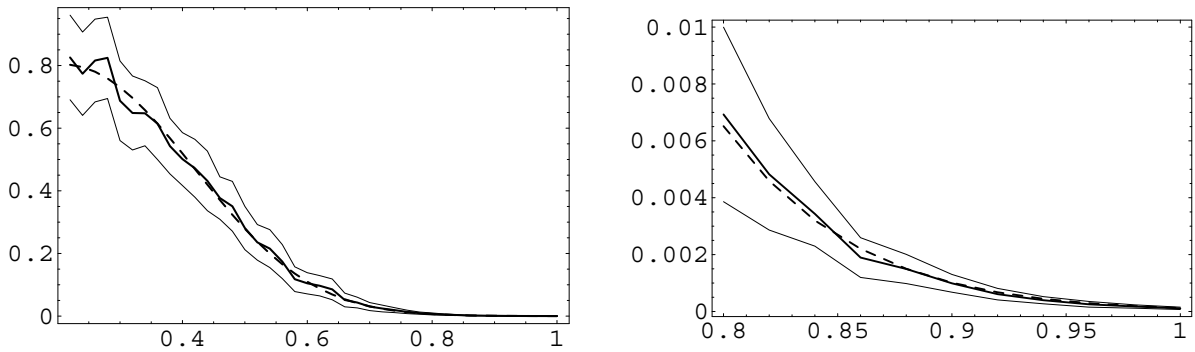


Figure 4.6 Exact solution, empirical mean and confidence intervals of the weighted scheme for the Mach number 10 using 100 averaging steps.

In these plots the dashed line represents the analytical solution (3.24), the thick solid line the empirical mean and the thin solid lines the confidence intervals. What is extremely remarkable is the high and homogeneous quality of the numerical solution. The right plot in **Figure 4.6** shows the same curves on the interval $[0.8, 1.0]$, i.e. close to the top boundary of the domain where the density becomes really low. The first acceptable numerical solution using constant weights can be obtained after 1600 averaging steps (which means that the computational time is 16 times larger).

Now we can compare the quality of the numerical solutions obtained using standard and weighted methods. In **Figure 4.7** we show the analytic curve (dashed line) and the confidence intervals for both weighted (thin lines) and standard schemes (thick lines) on the interval $[0.2, 1.0]$ (left plot) and on the interval $[0.8, 1.0]$ (right plot).

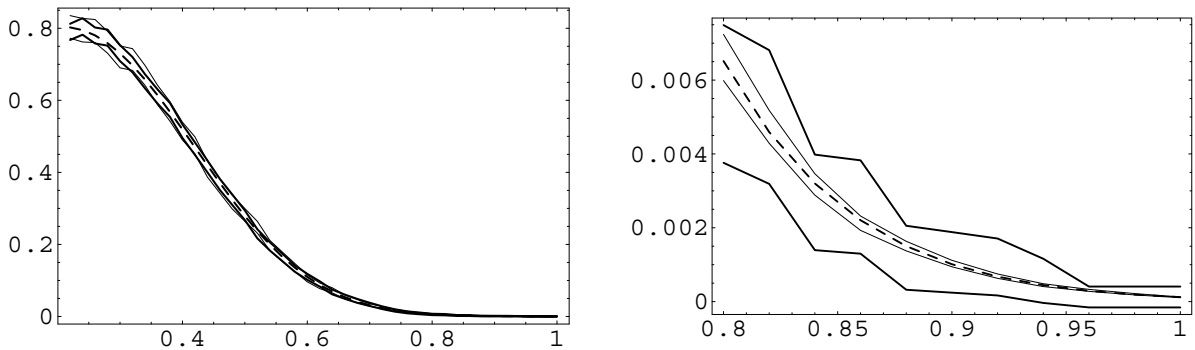


Figure 4.7 Exact solution and confidence intervals of the two methods for Mach number 10 using 1600 averaging steps.

There are some comments necessary. In the main stream the standard particle method is slightly better due to the fact that it sends all generated particles there. By contrast, the weighted scheme sends half of almost the same number of particles in the desired direction of the auxiliary stream. The situation changes drastically close to the top of the computational domain (right plot). The weighted scheme is much more precise here. We illustrate this fact in **Figure 4.8**. Here we show the quotient of the thickness of the confidence interval and of the analytic density for both methods.

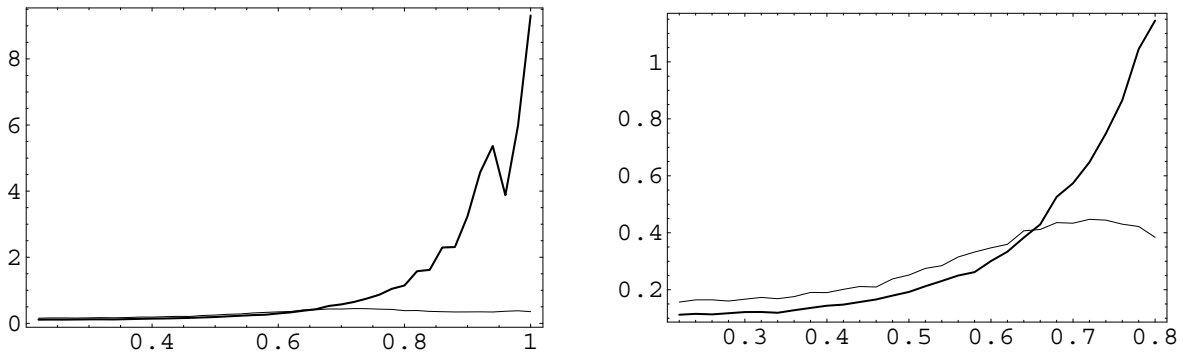


Figure 4.8 Quotients of the thickness of the confidence intervals of the two methods and of the exact solution for Mach = 10 using 1600 averaging steps.

The thick line represents the relative accuracy of the standard scheme while the thin line is the corresponding plot for the weighted scheme. The right plot in **Figure 4.8** shows the situation in the main stream. It is remarkable that the quality of the resolution of the weighted method remains almost constant compared to the standard scheme. The quality of the standard method decreases monotonically by leaving the main stream. On the other hand the weighted method begins to be affected by more particles arriving here because of the modelling of the auxiliary stream. Thus the relative quality of resolution using the weighted method is almost constant over the whole region.

The situation changes if we introduce collisions. The weighted method is more expensive because of complicated modelling of collisions, the appearance of new particles due to collisions, etc. A fair comparison of both methods can be done if we compare the computational time needed to achieve the same accuracy of the numerical solution. For the above example we do not have any advantage using weights. We obtain almost the same accuracy (except the points very close to the top boundary) if we use 6400 averaging steps of the weighted scheme and 25600 averaging steps of the standard scheme. These numbers of averaging steps were chosen so that the computational time for the two methods is almost the same.

One of the great advantages of our weighted method is that the number of particles artificially directed into the desired region is independent of the Mach number. If the density there is very low then the same number of particles having lower weights will arrive there. This is not so with the standard scheme, where the probability that even one particle having standard (large) weight will reach the desired region decreases rapidly with the increase in the Mach number.

Our next tests show the situation for Mach number 15. The density close to the top boundary is about 10^{-8} times ρ_{in} . For our specific setting of the standard weight that means that a particle will visit the region close to the top boundary once in every million averaging steps. It is clear that the corresponding computational time will be enormous. We performed this large test using 1638400 averaging steps for the standard scheme and 25600 for the weighted scheme. The mean free path was chosen as $\varepsilon = 0.2$. Thus the number of averaging steps was 64 times higher than for the weighted scheme. Since the weighted scheme needs a little less than four times more computational time per averaging step the whole computation was about 16 times faster using weighted particles.

The quality of the numerical solution is presented in **Figure 4.9**.

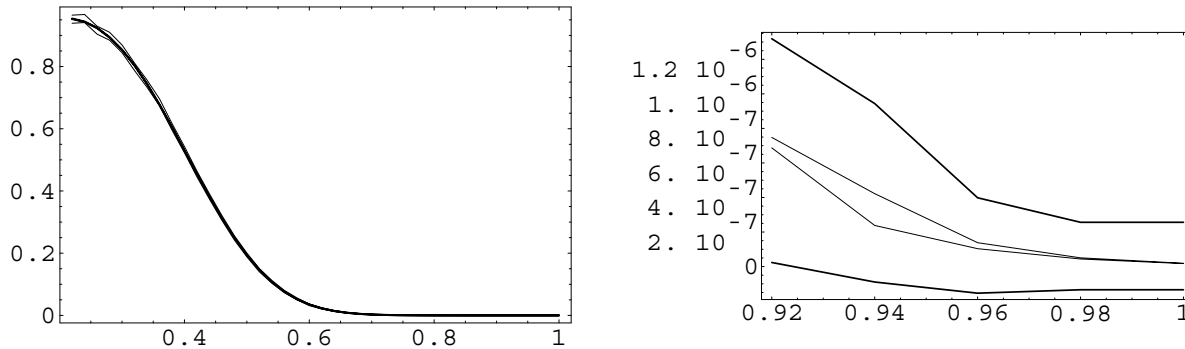


Figure 4.9 The confidence intervals of the two methods for Mach number 15 using 1638400 (standard) or 25600 (weighted) averaging steps.

We show the confidence bands for the two methods on the whole interval (left plot) and on the crucial interval $[0.9, 1.0]$ (right plot). It is clear to see that even having 16 times computational time, the standard particle scheme is still not in a position to deliver the accuracy of the weighted scheme. Note that a reasonable solution could be obtained with the weighted scheme using only 400 averaging steps, i.e. in less than 0.1% computational time.

5. Conclusions

In this paper we presented an extension of the stochastic weighted particle method by introducing a procedure for modelling the inflow boundary condition using weighted particles. The performance of the new procedure was tested in an example with two-dimensional physical space, where, dependent on the Mach number of the incoming flow, very strong density gradients appear. The geometry of our test problem is an extremely simplified model of the thin film deposition system considered in [2, Fig. 4].

The numerical results are very promising. In the calculation of a surface functional (flux through a plane) a gain factor of 140 in computing time was achieved for SWPM compared with the standard scheme. In the calculation of a volume functional (density along a line) this gain factor was even 1000. Here the functional to be calculated varied in a range from 1 to 10^{-7} .

These results are a preliminary step towards a precise calculation of the heating effect of the “hot top” formulated in the first part of Section 3. To deal with the full problem, procedures for the reduction of the number of simulation particles in regions of high density as described in [5] should be applied. Here no reduction was necessary, since the outgoing flow was strong enough.

Acknowledgments: The authors would like to thank G. A. Bird and I. D. Boyd for a number of very helpful discussions which motivated the test example of this paper. Support by the Volkswagen Foundation (RiP-program at Oberwolfach) is gratefully acknowledged.

References

- [1] G. A. Bird. *Molecular Gas Dynamics and the Direct Simulation of Gas Flows*. Clarendon Press, Oxford, 1994.
- [2] I. D. Boyd. Conservative species weighting scheme for the direct simulation Monte Carlo method. *J. of Thermophysics and Heat Transfer*, 10(4):579–585, 1996.
- [3] C. Cercignani, R. Illner, and M. Pulvirenti. *The Mathematical Theory of Dilute Gases*. Springer, New York, 1994.
- [4] H. Neunzert, A. Klar, and J. Struckmeier. Particle methods: theory and applications. In *ICIAM 95 (Hamburg, 1995)*, pages 281–306. Akademie Verlag, Berlin, 1996.
- [5] S. Rjasanow, T. Schreiber, and W. Wagner. Reduction of the number of particles in the stochastic weighted particle method for the Boltzmann equation. *J. Comput. Phys.*, 145(1):382–405, 1998.
- [6] S. Rjasanow and W. Wagner. A stochastic weighted particle method for the Boltzmann equation. *J. Comput. Phys.*, 124(2):243–253, 1996.
- [7] S. Rjasanow and W. Wagner. Numerical study of a Stochastic Weighted Particle Method for a model kinetic equation. *J. Comp. Phys.*, 128(1) : 351–362, 1996.
- [8] S. Rjasanow and W. Wagner. A generalised collision mechanism for stochastic particle schemes approximating Boltzmann type equations. *Computers Math. Applic.*, 35(1/2) : 165–178, 1998.
- [9] S. Tiwari. Coupling of the Boltzmann and Euler equations with automatic domain decomposition. *J. Comput. Phys.*, 144(2):710–726, 1998.